Scientific Research Publishing

Open Journal of Applied Sciences, 2025, 15(10), 3247-3263
https://www.scirp.org/journal/ojapps
ISSN Online: 2165-3925
ISSN Print: 2165-3917

Multi-Objective Optimization of Front Landing Gear Impact Based on Multivariate Nonlinear Regression

Jiahao Fu[1], Sen Hu[1], Bo Shao[2]

[1]School of Aeronautics and Astronautics, Sun Yat-sen University, Guangzhou, China
[2]School of Science and Technology, Hunan University of Technology, Zhuzhou, China
Email: 1242511980@qq.com

How to cite this paper: Fu, J.H., Hu, S. and Shao, B. (2025) Multi-Objective Optimization of Front Landing Gear Impact Based on Multivariate Nonlinear Regression. *Open Journal of Applied Sciences*, **15**, 3247-3263.
https://doi.org/10.4236/ojapps.2025.1510209

Received: September 19, 2025
Accepted: October 24, 2025
Published: October 27, 2025

Abstract

To address the multicoupling effects of stress response in UAV landing gear during touchdown, this study employs a multivariate nonlinear regression approach for multi-objective optimization design of the UAV nose landing gear. Theoretical analysis of the landing process first identified stress responses relative to shock absorber stiffness, damping coefficient, and strut angle as optimization objectives. Using ADAMS and Simulink co-simulation, landing stress responses under varying parameter combinations were quantified. Subsequently, a multivariate nonlinear regression model derived the analytical solution for minimum stress under the coupled influence of all three factors. Physical prototype landing tests ultimately validated the accuracy of the optimized results. These findings provide a theoretical foundation for designing lightweight yet high-reliability UAV landing gear.

Keywords

Landing Gear, Multivariate Nonlinear Regression, Landing Stress Response, ADAMS-Simulink Coupling

1. Introduction

At the moment of aircraft touchdown, the massive impact load sweeps through the nose landing gear system like a tidal wave, presenting a severe test for both structural strength and crew comfort [1] [2]. The peak impact force and its time-domain characteristics not only directly correlate with the stress levels of critical components such as the landing gear strut and wheel axle, but also affect the buffer system's sealing effectiveness, the aircraft's longitudinal overload, and even the airframe's flutter characteristics [3]. Excessive impact can potentially cause immediate damage such as local plastic deformation or oil overheating causing seal failure, and can also trigger long-term issues like structural fatigue and fastener loosening during repeated landings, posing substantial threats to flight safety. Therefore, precisely anticipating and effectively controlling the nose landing gear's touchdown impact response at the design stage is a core proposition for achieving its high reliability and long service life [4].

The nose landing gear is a highly coupled nonlinear dynamic system whose touchdown impact response is governed by complex covariant interactions among multiple critical design parameters, including structural stiffness, damping characteristics, and strut inclination angle [5] [6]. Conventional univariate analysis or empirical formulations are insufficient to characterize the nonlinear synergistic mechanisms through which these parameters collectively determine the resultant impact force distribution [7]. For instance, minor strut inclination adjustments simultaneously alter impact load transmission paths and vertical load component proportions while modulating ground-tire contact forces; structural stiffness settings fundamentally determine system natural frequencies and airframe load-sharing patterns; while damping coefficient configurations dictate the kinetic-to-thermal energy conversion rate and efficiency during landing energy dissipation [8]. These intricate coupling effects render traditional trial-and-error design methodologies inadequate for achieving globally optimal performance [9].

Multivariate nonlinear regression modeling provides a robust mathematical framework for comprehending and optimizing such multi-objective coupled parameter systems [10]. This methodology effectively integrates stiffness matrices, nonlinear damping models, strut spatial orientation angles [11], and essential initial touchdown conditions to construct precise nonlinear mappings between input parameters and multidimensional output targets—e.g., peak impact forces, airframe pitch angular velocity, and energy dissipation uniformity—within high-dimensional solution spaces. By revealing critical parametric sensitivity laws and interaction mechanisms within its data-driven black-box architecture, the model enables intelligent exploration of optimized solution domains across multivariate parameter spaces [12].

This study accordingly establishes an integrated multi-objective optimization framework for nose landing gear touchdown impact, unifying the core parameter triad of stiffness-damping-strut inclination [13]. The methodology centers on employing multivariate nonlinear regression to construct high-fidelity impact response prediction models, synergistically fused with intelligent optimization algorithms to co-optimize three objectives: impact force peak suppression, ride quality enhancement (minimizing vertical acceleration and pitch oscillations), and energy dissipation stability [14]. It achieves Pareto-optimal design configurations under complex operational scenarios. This research not only delivers an empirically validated computational framework for gear dynamics design but establishes theoretical and technological foundations for systematically improving aircraft landing safety, structural durability, and occupant comfort—providing critical support for next-generation airframe lightweighting and performance advancement [15].

2. Theoretical Analysis of UAV Landing

2.1. UAV Landing Analysis

Maintaining pitch-axis moment balance prior to touchdown constitutes a critical design consideration in aircraft flight control systems. During this phase, the line of action of force C (incorporating empennage contributions) must intersect the center of gravity while establishing equilibrium with the resultant of gross weight G and axial force A, thereby attaining zero net force to prevent excessive pitching motion of the airframe.

$$N = G + A \tag{1}$$

In Equation (1), N represents the resultant normal force acting on the aircraft, G denotes gravity, and A signifies the axial force acting on the aircraft.

At touchdown instant, the normal force N, axial force A, and gravity G remain unchanged and equilibrated with zero resultant force. When referencing the main gear as the pitch axis, moments induced by these forces remain zero, confirming pitch equilibrium upon ground contact. Friction and vertical reaction forces at the main gear produce no moments due to collinear action with the pitch axis, ensuring pitch stability. As airspeed decays, diminished N and A progressively disrupt moment equilibrium, generating a nose-down moment. This increasing nose-down moment induces rotation around the main gear until nose-wheel touchdown initiates pitch balance transition. The main gear track is primarily determined by ground roll stability requirements. When featuring high wing aspect ratio causing significant roll inertia, adequate transverse span becomes critical to generate sufficient restoring roll moment during single-gear touchdown incidents induced by taxiing on uneven terrain, thereby preventing ground rollover. Concurrently, a properly designed track requires substantial lateral overturning moment to induce rolling when both mains are grounded, ensuring anti-rollover stability throughout landing and taxi phases (see **Figure 1**).

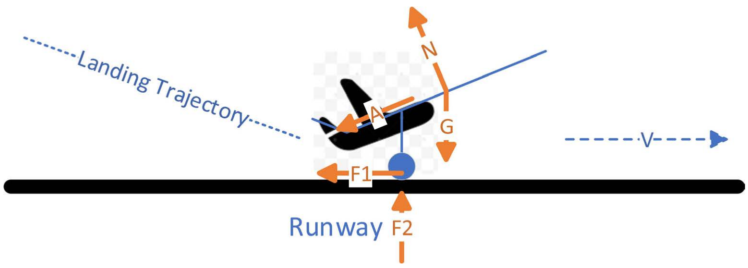

Figure 1. Schematic diagram of UAV landing.

During aircraft landing, the main gear primarily absorbs the impact energy generated by ground contact, necessitating not only sufficient energy absorption capacity but also superior resilient deformation resistance. This ensures effective damping of severe landing impacts while preventing excessive deformation. Such characteristics are critical for maintaining landing safety and stability, particularly under varying terrain conditions, where the main gear's damping performance and elastic design directly govern ride comfort and operational integrity.

2.2. Landing Gear System Touchdown Dynamics Model

Per d'Alembert's principle, the dynamic equations are derived as:

1) Rigid-body longitudinal motion

$$M_1\ddot{q}_1 = 2Q_V\sin(\beta) + 2Q_H\cos(\beta) - (L - M_1 g)\sin(q_3) \tag{2}$$

Equation (2), M_1 denotes the isolated airframe mass excluding the non-sprung mass of the main landing gear, q_1 represents the rigid-body longitudinal degree of freedom, Q_V signifies the axial force parallel to the strut at axle A, Q_H indicates the radial force perpendicular to the strut axis at axle A, and L defines the aircraft lift force.

2) Rigid-body vertical motion

$$M_2\ddot{q}_2 = 2Q_V\cos(\beta) + 2Q_H\sin(\beta) - (L - M_1 g)\cos(q_3) \tag{3}$$

In Equation (3), M_2 denotes the isolated airframe mass excluding the non-sprung mass of main landing gear, and q_2 represents the rigid-body heave degree of freedom.

3) Rigid-body pitching motion

$$M_3\ddot{q}_3 = 2(L_1 + L_2) \tag{4}$$

$$L_1 = -\left[Q_H - M_5 g\sin(q_3 + \alpha_0)\right](DL - S_M) \tag{5}$$

$$\begin{aligned} L_2 = &-x_B\left\{\left[Q_V + M_5 g\cos(q_3+\alpha_0)\right]\cos\beta - \left[Q_H - M_5 g\sin(q_3+\alpha_0)\right]\sin\beta\right\} \\ &-(Z_C - Z_B)\left\{\left[Q_V + M_5 g\cos(q_3+\alpha_0)\right]\sin\beta + \left[Q_H - M_5 g\sin(q_3+\alpha_0)\right]\cos\beta\right\} \end{aligned} \tag{6}$$

$$L - M_1 g = 2M_5 g \tag{7}$$

$$DL = (Z_B - Z_A)/\cos\beta \tag{8}$$

In Equations (4) to (8), L_1 denotes the moment about Point B of forces applied at Point A, L_2 represents the moment about the center of gravity of the unmanned aircraft of forces applied at Point B, q_3 indicates the rigid-body pitching degree of freedom, M_3 signifies the pitch moment of inertia of the isolated unmanned aircraft mass excluding main landing gear lower unsprung components, M_5 designates the mass of each main landing gear lower unsprung component, x_B defines the x-coordinate of landing gear attachment Point B, and Z_A, Z_B, Z_C specify the z-coordinates of landing gear attachment Points A, B, and C respectively.

4) Wheel spin-up dynamics

$$M_4\ddot{q}_4 = D_T\left(R_M - \delta_M/2\right) \tag{9}$$

In Equation (9), M_4 denotes the rotational inertia of each main landing gear wheel assembly, $\left(R_M-\delta_M/2\right)$ signifies the effective rolling radius of the wheel, and q_4 indicates the wheel spin-up rotational degree of freedom.

5) Unsprung mass vertical travel of landing gear

$$M_5\ddot{q}_5=Q_V-\left(F_T-M_5g\right)\cos\left(\beta+q_3\right)-D_T\sin\left(\beta+q_3\right) \tag{10}$$

In Equation (10), q_5 denotes the vertical degree of freedom of the main landing gear lower unsprung mass, F_T signifies the tire-ground normal reaction force, and D_T represents the tire-ground tangential friction force.

6) Unsprung mass fore-aft motion of landing gear

$$M_6\ddot{q}_6=-Q_H-\left(F_T-M_6g\right)\sin\left(q_3+\beta\right)-D_T\cos\left(q_3+\beta\right) \tag{11}$$

In Equation (11), q_6 denotes the fore-aft degree of freedom of the main landing gear lower unsprung mass, and M_6 represents the mass per lower unsprung component of each main landing gear.

2.3. Selection of Nose Landing Gear Optimization Parameters

The strut stiffness and damping parameters are core elements affecting landing performance, jointly determining stroke length which directly governs impact energy absorption efficiency and transmission characteristics as shown in **Figure 2**. Increased stiffness may shorten stroke but exacerbate landing gear stress peaking effects, while enhanced damping significantly mitigates stress peaks through energy dissipation. The strut installation angle modulates impact force decomposition mechanisms, critically governing the proportion of vertical to lateral force components and profoundly influencing structural stability and dynamic load distribution. Nose landing gear optimization must focus on three key variables: damping parameters, stiffness coefficients, and strut inclination angle. Synergistic optimization of these parameters balances impact absorption efficacy with system stability. This study will optimize nose gear stiffness, damping, and strut angle to minimize stress peaks in UAV landings.

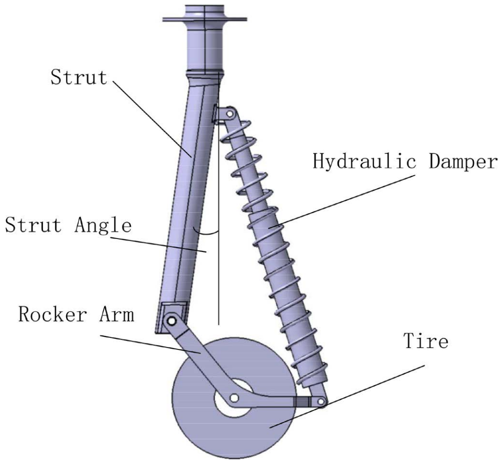

Figure 2. Front landing gear parameters.

3. Unmanned Aerial Vehicle Landing Simulation

3.1. Landing Gear Structure and Configuration

Research subject: 300 kg fixed-wing UAV with main/nose gear CG distance ratio of 2:1 (**Figure 3**). Landing sequence: main wheels (aft gear) contact first, absorbing primary impact loads; nose gear subsequently contacts, dissipating partial energy while transferring the remainder to the airframe. Nose landing gear assembly comprises strut, torque links, shock absorber, and tire. High-strength aluminum alloy construction ensures structural integrity with minimized weight. Tricycle configuration positions main gears aft of CG and nose gear under the nose section, enhancing ground steering response and maneuverability during landing.

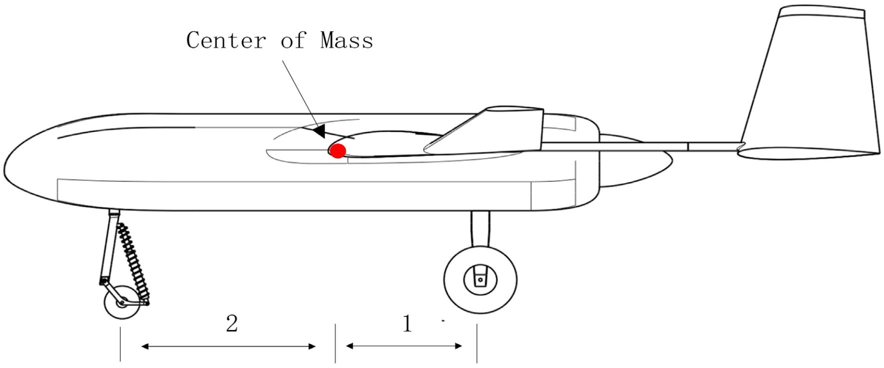

Figure 3. UAV landing gear configuration.

3.2. Adams-Simulink Co-Simulation

During UAV landing simulation, primary variables include force/moment variations on the airframe and velocity transitions. Adams-generated body-axis velocities feed into Simulink as inputs. In wind-axis coordinates, aerodynamic coefficients exhibit nonlinear dependence on α (angle of attack) and β (sideslip angle) through their 1st, 2nd, and 3rd-order terms, while also correlating significantly with aileron deflection (cmd1) and rudder angle (cmd2). Thus, outputs comprise six aerodynamic coefficients—lift coefficient C_L, drag coefficient C_D, Side force coefficient C_Y, roll moment coefficient C_l, pitch moment coefficient C_m, yaw moment coefficient C_n —computed from α, β (including higher-order polynomials), and control surface deflections in wind-axis reference. Prior to Adams reintegration, these wind-axis forces/moments undergo coordinate transformation to body-axis via stability-axis intermediate frame using the rotation matrix defined by aerodynamic angles.

$$\begin{bmatrix} X_b \\ Y_b \\ Z_b \end{bmatrix} = \begin{bmatrix} 1 & \sin(\alpha) & 0 \\ 0 & \cos(\alpha) & 0 \\ 0 & 0 & 1 \end{bmatrix} \begin{bmatrix} X_s \\ Y_s \\ Z_s \end{bmatrix} \tag{12}$$

In Equation (12), X_b, Y_b, Z_b denote the body-frame axes, while X_s, Y_s,

Z_s represent the stability axes.

The rotation from the stability frame to the wind frame is governed by the sideslip angle β, defined as the angle between the aircraft's longitudinal axis and the relative wind direction; this transformation is represented by the following matrix:

$$\begin{bmatrix} X_s \\ Y_s \\ Z_s \end{bmatrix} = \begin{bmatrix} 1 & \sin(\beta) & 0 \\ 0 & \cos(\beta) & 0 \\ 0 & 0 & 1 \end{bmatrix} \begin{bmatrix} X_\omega \\ Y_\omega \\ Z_\omega \end{bmatrix} \tag{13}$$

In Equation (13), X_ω, Y_ω, Z_ω denote the body-frame axes.

by composing the two transformations (from body frame to stability frame and stability frame to wind frame) via matrix multiplication, the complete transformation from body frame to wind frame is obtained:

$$\begin{bmatrix} X_b \\ Y_b \\ Z_b \end{bmatrix} = \begin{bmatrix} 1 & \sin(\alpha) & 0 \\ 0 & \cos(\alpha) & 0 \\ 0 & 0 & 1 \end{bmatrix} \begin{bmatrix} \cos(\beta) & 0 & \sin(\beta) \\ 0 & 1 & 0 \\ -\sin(\beta) & 0 & \cos(\beta) \end{bmatrix} \begin{bmatrix} X_\omega \\ Y_\omega \\ Z_\omega \end{bmatrix} \tag{14}$$

This composite transformation matrix establishes the relationship between the body-fixed frame and the wind frame by accounting for both angle of attack α and sideslip angle β.

The converted aerodynamic forces and moments are then applied as inputs to Adams. Through multibody dynamics simulation, the vehicle's dynamic response—including velocity, attitude, acceleration, and other parameters across varying flight conditions—is solved. These outputs represent real-time dynamic responses rather than static values. By feeding back simulation results (e.g., velocity and attitude) as inputs to the aerodynamic model, a closed-loop control system is formed (schematically illustrated in **Figure 4**). This closed-loop system continuously adjusts inputs to dynamically update aerodynamic force/moment distributions, enabling the simulation to capture the aircraft's real-world landing performance in complex environments. Specifically, variations in velocity, angle of attack, and attitude alter flow characteristics, thereby affecting distributions of lift, drag, and moment loads. The closed-loop system iteratively refines these inputs to ensure accurate representation of nonlinear behavior and dynamic responses across flight regimes, particularly under high-angle-of-attack or unstable conditions where aerodynamic-structural interactions emerge. The overall methodology is depicted in.

3.3. Simulation Procedure

1) Contact Settings

In ADAMS, contact exhibits strongly nonlinear behavior during the simulation of collisions, friction, sliding, or compression between objects. Improper definition may lead to computational non-convergence and increased solving time. This simulation neglects interactions between wings, tail wings, and the fuselage, modeling their connections as fixed joints. For steering capability, the nose landing gear is allowed to rotate around its attachment point to the fuselage via a

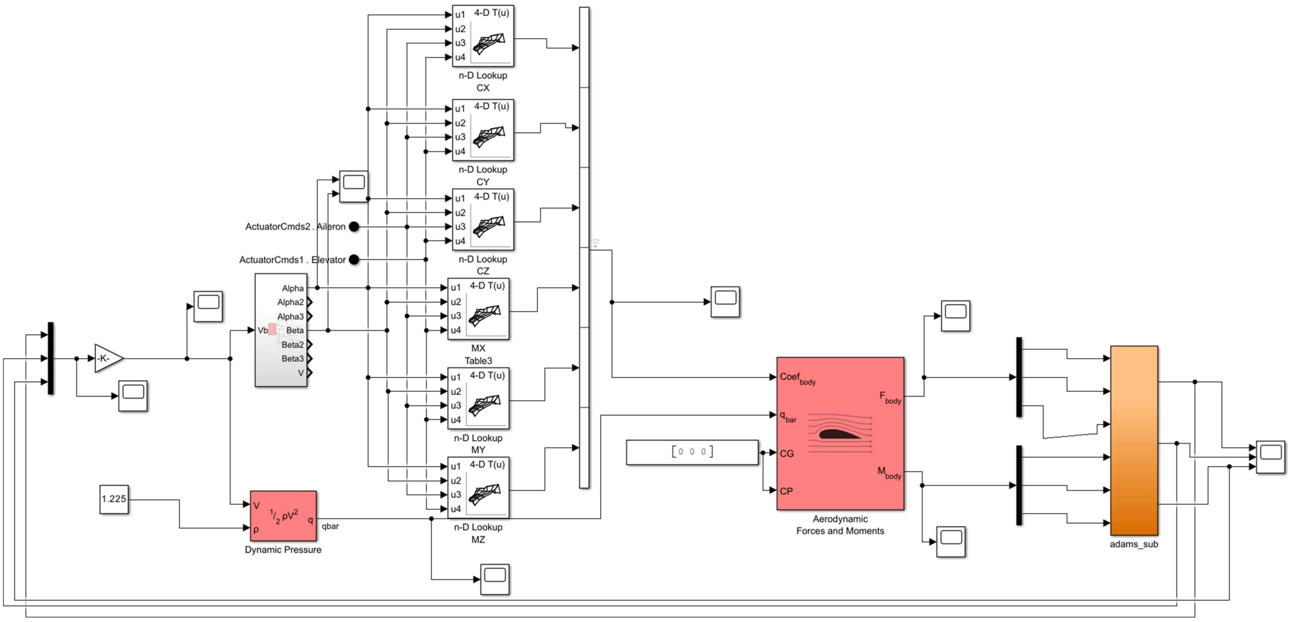

Figure 4. Schematic diagram of cosimulation principle.

revolute joint. During landing, the strut can pivot perpendicular to the flight direction around its hinge. Energy absorption is achieved through shock absorber compression and rear landing gear deformation, with revolute joints connecting the strut-to-rocker, rocker-to-damper, and damper-to-strut. Wheel assemblies are attached to the airframe via revolute joints to simulate landing dynamics, as shown in **Figure 5**.

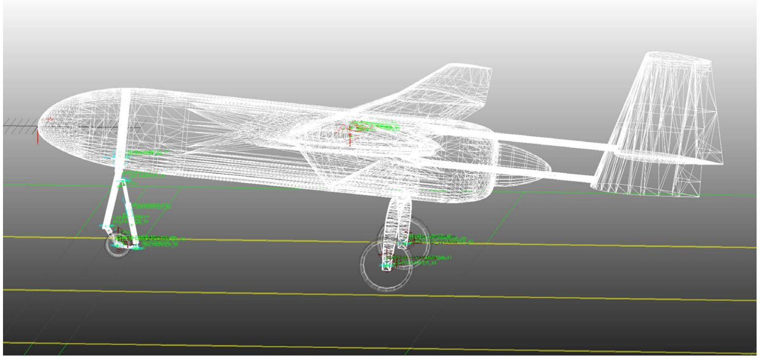

Figure 5. Schematic diagram of structural contact.

2) Material Setting

In ADAMS, the material configuration for the landing gear emphasizes dynamic characteristics and load-transfer mechanisms. Based on rigid-body dynamics assumptions, material definitions exclude strain energy calculations, focusing instead on mass distribution, moment of inertia, and contact force computation. No significant plastic deformation was observed in the front and rear structures under landing impact conditions. Isotropic aluminum alloy and orthotropic carbon-fiber composites were used for mechanical modeling, characterized by three key parameters: density, Young's modulus, and Poisson's ratio. This parametric approach ensures accurate simulation of dynamic load transfer during landing while preserving rigid-body motion fidelity. Simulation validation confirms that this method reliably captures the landing gear's dynamic response under impact loads, with inertial property errors within 5% compared to experimental data in Table 1.

Table 1. Material parameters.

Name	Name	Parameters
Nose Landing Gear	Density (g/cm^3)	2.81
	Young's Modulus (GPa)	71.7
	Poisson's Ratio	0.33

3) State and Load Settings

The entire UAV fuselage is configured at a 5-degree angle relative to the horizontal line, ensuring a 5-degree pitch angle during landing. A longitudinal thrust force F1 is applied at the UAV's center of mass to achieve a landing horizontal velocity of 32 m/s, while a vertical thrust force F2 is applied to achieve a landing vertical velocity of 2.5 m/s, as illustrated in Figure 6. Additionally, forces and moments along the x-, y-, and z-axes are applied at the UAV's center of mass, imported from aerodynamic calculations performed in Simulink.

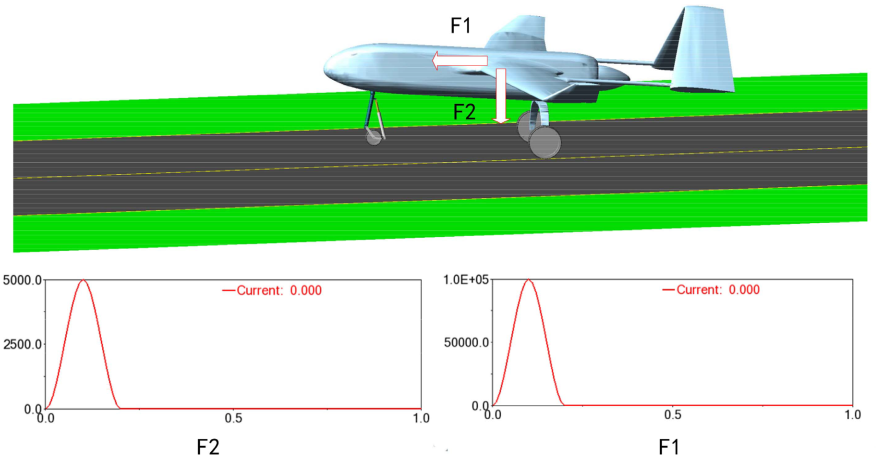

Figure 6. Schematic diagram of load configuration.

4) Tire and Road Settings

In Adams, to simulate different road types and account for potential tire sideslip during UAV landing, this study employs the Magic Formula Tire Model (MFTyre). This model accurately captures the tire's mechanical response under complex contact conditions, particularly under impact loads. The front wheel moments of inertia are set to $I_{xx} = I_{yy} = 0.003\,\mathrm{kg \cdot m^2}$, $I_{zz} = 0.006\,\mathrm{kg \cdot m^2}$, with a mass of 0.84 kg, while the rear wheel moments of inertia are

$I_{xx} = I_{yy} = 0.067\ \text{kg} \cdot \text{m}^2$, $I_{zz} = 0.134\ \text{kg} \cdot \text{m}^2$, with a mass of 1.5 kg. These configurations ensure precise simulation of tire dynamic behavior during landing, enhancing result reliability in Table 2.

Table 2. Tire parameters.

Tire	Application Conditions
Magic Formula Tire Model	Switchable between steady-state and non-steady-state modes, accounts for gyroscopic coupling during high-speed rotation, interactions between sideslip and longitudinal slip, and camber effects.
Pacejka89, Pacejka94	Steady-state sideslip model, not suitable for transient conditions
PAC2002 Model	Effective up to 8 Hz, primarily used for handling and stability simulations
PAC MC Model	Designed for motorcycle tires (effective up to 8 Hz), suitable for large camber angles
Fiala Model	Beam-on-elastic-foundation model, neglects camber and relaxation length effects
UA Model	Accounts for coupled slip (lateral/longitudinal) interactions, camber effects, and relaxation lengths—delivers high accuracy with minimal input parameters

The road-tire interaction uses Adams' 3D volumetric contact model, which computes intersection volume between tire and road surfaces. The road is represented by discrete triangular facets, exemplified by a surface composed of six nodes (1 - 6) forming four triangular elements (A, B, C, D), each with outward unit normal vectors. Tires are modeled as cylindrical segments. This approach enables simulation of scenarios like curb strikes, potholes, or rough/irregular terrain. The current simulation adopts the road_3d_smooth road model (Figure 7).

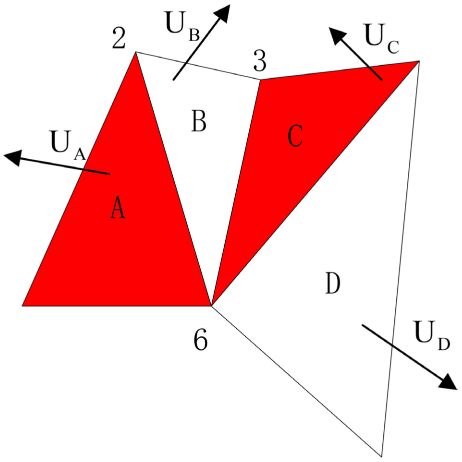

Figure 7. Schematic diagram of road surface discretization.

5) Load Import from Simulink to Adams

The aerodynamic coefficients (lift, drag, side force, roll/pitch/yaw moments) calculated in Simulink are transformed into body-frame forces/moments and applied as input loads in Adams. As shown in Figure 8, the resultant forces are: drag (X-axis) = 375 N, lift (Y-axis) = 2350 N, side force (Z-axis) = 96 N. The moments are: roll (X-axis) = 1.05 × 10^5 N·m, pitch (Y-axis) = 0.98 × 10^5 N·m, yaw (Z-axis) = 2.79 × 10^5 N·m.

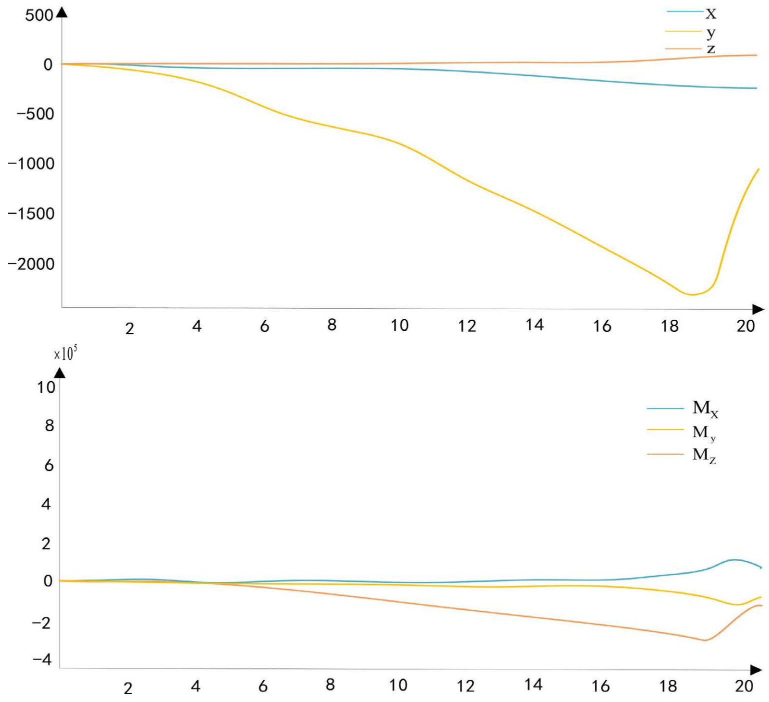

Figure 8. Schematic diagram of load import.

3.4. Simulation Results Analysis

During calculations, the principle of single variable control was applied. When investigating damper damping, the stiffness of the buffer and the strut angle were held constant; when investigating buffer stiffness, the damper damping and the strut angle were held constant; when investigating the strut angle, the stiffness of the buffer and the damper damping were held constant; variables adopted gradient-based stepwise values, with results as follows (in **Table 3**):

Table 3. Schematic summary of simulation results.

Damping (N*s/mm)	0.5	1	2	3	4	5	6	7	8	7
Damping versus stress (MPa)	66.8	65.9	64.4	63.8	63.2	62.9	62.6	62.4	62.3	62.2
stiffness (N/mm)	10	20	30	40	50	60	70	80	90	100
Stiffness versus stress. (MPa)	60.1	61	62.2	62.8	63.2	64.8	67.8	68.1	69.3	69.8
strut angle (˚)	2.5	5	7.5	10	12.5	15	17.5	20	22.5	25
strut angle versus stress (MPa)	69.3	67.2	65.1	62.8	60.2	58.3	57.8	55.9	55.5	55.3

4. Multi-Objective Optimization Computation

4.1. Optimization Methodology

1) Fundamental System Model

Multivariate nonlinear regression is a statistical modeling method used to describe complex nonlinear relationships between multiple independent variables (explanatory variables) and a dependent variable (response variable); unlike multivariate linear regression, its mathematical form cannot be expressed as a linear combination of the independent variables but instead involves complex nonlinear relationships such as exponential, logarithmic, power functions, fractional, and trigonometric functions, finding widespread application in fields including engineering modeling, financial forecasting, biostatistics, and machine learning, with its general mathematical expression being:

$$y = f\left(x_1, x_2, \cdots, x_n; \theta\right) + \varepsilon \tag{15}$$

In the Equation (15), $f\left(x\right)$ represents a nonlinear function, y is the dependent variable, $x_1, x_2, \cdots, x_n$ is the set of independent variables, θ denotes the parameter vector to be estimated, and ε signifies the error term.

2) SLSQP Optimization Algorithml

SLSQP (Sequential Least Squares Programming) is an iterative algorithm designed for constrained nonlinear optimization problems, with its core steps including: Objective function approximation: At the current iteration point x_k, the objective function $f\left(x\right)$ is approximated as a quadratic function using a second-order Taylor expansion:

$$f\left(x\right) \approx f\left(x_k\right) + \nabla f\left(x_k\right)^{\mathrm{T}}\left(x - x_k\right) + \frac{1}{2}\left(x - x_k\right)^{\mathrm{T}} \nabla^2 f\left(x_k\right)\left(x - x_k\right) \tag{16}$$

where ∇f and $\nabla^2 f$ represent the gradient and Hessian matrix, respectively.

Constraint linearization: Nonlinear constraints $g_i\left(x\right) \le 0$ are approximated as linear constraints using a first-order Taylor expansion:

$$g_i\left(x\right) \approx g_i\left(x_k\right) + \nabla g_i\left(x_k\right)^{\mathrm{T}}\left(x - x_k\right) \le 0 \tag{17}$$

At each iteration, a quadratic programming (QP) subproblem is solved to obtain a new iteration point x_{k+1}, The algorithm flowchart is as follows (in **Figure 9**).

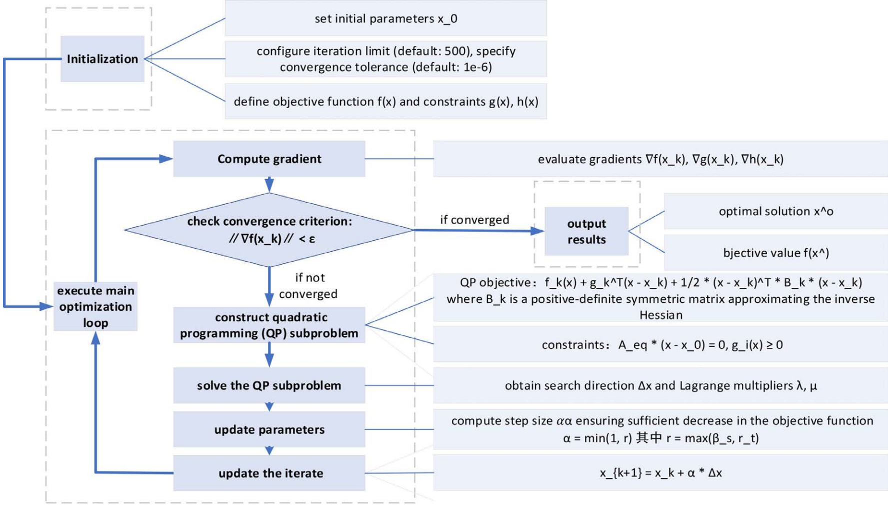

Figure 9. Flow chart of the SLSQP algorithm.

4.2. Multi-Objective Optimization Processing

Defining the stiffness x_1, damping x_2, and strut angle x_3 of the nose landing gear as variables, these parameters and stress data are fitted to a multivariate nonlinear regression model, yielding both first-order and second-order fitted surfaces as shown below. The coefficient of determination for the first-order fit R^2 is 0.907, while for the second-order R^2 fit it improves to 0.940, indicating that the second-order model more accurately captures the underlying data trend, with results presented in **Figure 10**. Therefore, the second-order fitted curve is selected as the final model, whose fitted function expression is:

$$\begin{aligned} y = & -2.53x_1^2 + 6.08x_2^2 + 8.46x_3^2 - 0.47x_1x_2 + 0.98x_1x_3 \\ & + 2.29x_2x_3 + 8.37x_1 - 5x_2 - 16.20x_3 + 62.85\times 10^6 \end{aligned} \tag{18}$$

The constraint conditions are:

$$\begin{cases} 1\times 10^4 \le x_1 \le 1\times 10^5 \\ 500 \le x_1 \le 1\times 10^4 \\ 2 \le x_1 \le 25 \end{cases} \tag{19}$$

The calculation shows the minimum force F_min 55.01 × 10^6 Pa, Stiffness = 25 N/mm, Damping = 1.5 N*s/mm, Angle = 10˚.

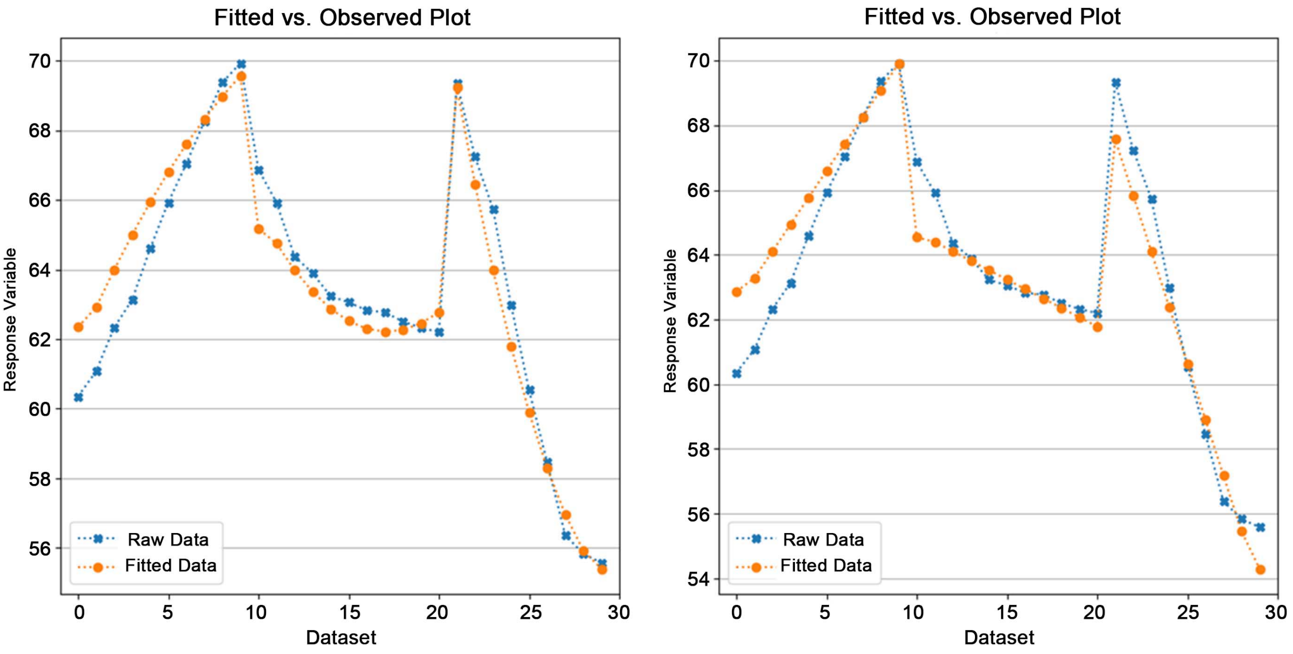

Figure 10. Fitting diagram of optimization parameters for the nose landing gear.

5. Experimental validation

5.1. Test Bench Design

The experimental setup consists of three parts: a landing gear fixture, a stress tester, and pressure sensors, as illustrated in the figure. It is designed to evaluate the peak stress and stress response of the front and rear landing gears under various optimized parameters, while validating the theoretical numerical calculations conducted earlier. This experiment eliminates external interference factors, focusing solely on the influence of structural parameters before and after optimization on impact forces and stress distribution.

The front and rear landing gears were scaled down to a 1:8 ratio and fabricated into physical models to simulate the landing gear system. The landing gear fixture is used to secure the landing gear and adjust its landing attitude, ensuring repeatability and accuracy during the experiments. Pressure sensors measure the impact pressure generated upon landing, while the stress tester records the stress distribution of the landing gear under impact loads. By testing landing gears with different parameters, as shown in **Figure 11**, the accuracy of the numerical simulations is verified.

At the beginning of the experiment, the front and rear landing gears optimized under different parameters are first secured to their respective landing gear fixtures, with the parameters shown in the chart, ensuring they are at the same initial height to guarantee consistency in release conditions. Subsequently, the landing gears are allowed to free-fall from the same height, and the measurements from the pressure sensors are recorded. If significant deviations exist in the pressure sensor readings, the release height or other experimental parameters should be adjusted until the sensors display consistent impact forces, ensuring that the experiment only studies the influence of landing gear optimization parameters on force transmission, without interference from height or external factors (in **Table 4**).

Table 4. Landing gear optimization parameters.

Name	Pre-optimization Parameters	Post-optimization Parameters
Nose Landing Gear	Stiffness: 40000 N/m Damping: 2500 N*s/m Strut angle: 8˚	Stiffness: 25000 N/m Damping: 1500 N*s/m Strut angle: 10˚

Once the pressure gauge measurements stabilize, strain gauges are affixed to key load-bearing areas of both front and rear landing gears, and the units are released from the adjusted height to measure stress variations under different optimization parameters. During repeated trials, the stress response impacts of different optimization designs on the landing gears are recorded, and analysis is conducted to assess whether the optimized designs effectively reduce stress concentrations and improve the damping performance of the landing gears. (**Figure 11**)

5.2. Experimental Results and Comparative Analysis before & after Optimization

5.2.1. Experimental Results

The stress measurement of the nose landing gear prior to optimization was 17.52 MPa, whereas after structural and material parameter optimizations, this value

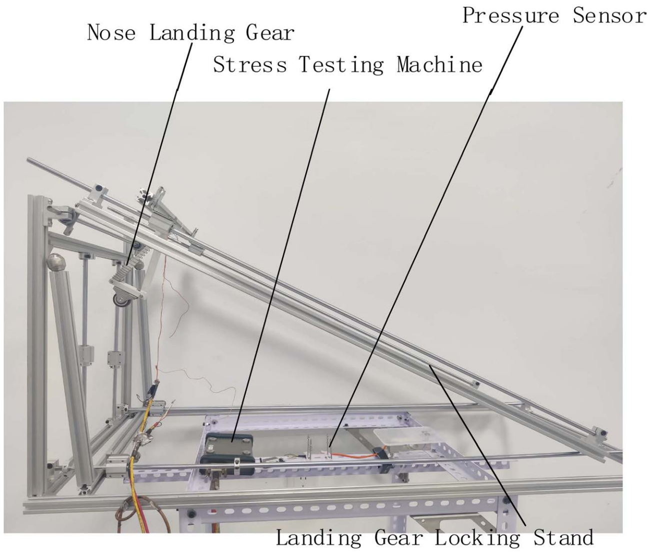

Figure 11. Landing gear stress testing experimental setup.

decreased to 13.96 MPa, representing a reduction of approximately 20.96%,as shown in **Figure 12**. This substantial stress reduction confirms that optimizing the geometric configuration, support structure, and damping system of the nose landing gear not only improved load distribution but also significantly enhanced overall impact resistance.

The optimized design achieves more uniform dissipation of peak landing stresses, thereby mitigating localized stress concentrations and reducing fatigue failure risks caused by excessive loading—ultimately extending the landing gear's operational lifespan. Moreover, this stress reduction contributes to improved stability and safety during UAV landings, establishing a solid foundation for further structural enhancements and performance upgrades.

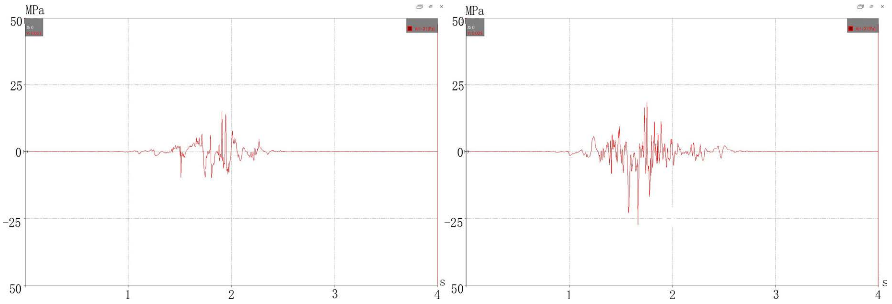

Figure 12. Rear landing gear test experimental data.

5.2.2. Comparative Analysis before and after Optimization

Comparative analysis between simulation results and experimental data confirms significant and consistent performance improvements in both the nose and main landing gears under the multi-objective optimization scheme, effectively validating the numerical simulation model's accuracy and reliability while demonstrating the optimization method's capability to achieve substantial reductions in overall stress peaks while maintaining balanced structural stiffness, energy absorption efficiency, and load distribution characteristics. The optimized landing gear assemblies exhibit more uniform stress distributions and lower transient peak stresses during landing operations, indicating successful mitigation of localized stress concentrations and corresponding reductions in impact-induced fatigue risks, thereby enhancing operational lifespan and system stability. The close agreement between experimental measurements and computational results further substantiates the practical feasibility of this multi-objective optimization strategy for engineering applications, providing robust theoretical and empirical foundations for UAV landing system design. In conclusion, comprehensive simulation-experimental verification confirms that the optimized landing gear configuration achieves ideal stress peak management performance, establishing a reliable technical foundation for ensuring safe UAV landings under complex operational conditions (in Table 5).

Table 5. Data comparison.

Category	Simulation Optimization Rate	Experimental Optimization Rate
Nose Landing Gear	20.58%	20.96%

6. Conclusions

Based on a multivariate nonlinear regression methodology, this study addresses the multi-coupled problem of landing stress response to optimize the UAV landing gear impact. Key conclusions are:

1) Aided by theoretical landing dynamics analysis and high-fidelity ADAMS/Simulink co-simulation datasets, the developed regression model effectively resolves the coupling mechanisms among stiffness, damping, and strut inclination;

2) Numerical optimization identifies the minimal structural stress at stiffness = 25 N/mm, damping coefficient = 1.5N·s/m, and strut angle = 10˚, with experimental validation confirming ≤ 0.5% deviation in stress predictions.

Conflicts of Interest

The authors declare no conflicts of interest regarding the publication of this paper.

References

[1] Liang, Y., Chin, P., Sun, Y. and Wang, M. (2021) Design and Manufacture of Composite Landing Gear for a Light Unmanned Aerial Vehicle. *Applied Sciences*, **11**, Article 509. https://doi.org/10.3390/app11020509

[2] Sivakumar, S., Ganapathy Subramanian, L.R. and Giridharan, V. (2024) Shimmy Vibration Analysis of Unmanned Aircraft Coupled with Landing Gears. *Journal of Mechanical Science and Technology*, **38**, 137-147. https://doi.org/10.1007/s12206-023-1211-1

[3] Çabuk, N. (2023) Design and Experimental Validation of an Adaptive Landing Gear for Safe Landing on Uneven Grounds of VTOL UAVs in the Context of Lightweight

and Fast Adaptations. *Arabian Journal for Science and Engineering*, **48**, 12331-12344. https://doi.org/10.1007/s13369-023-07731-x

[4] Lu, J., Nie, W., Ma, Y. and Li, X. (2020) Analysis Nonlinear Mechanical Characteristics Analysis of a UAV Landing Gear Shock Absorber. *Journal of Physics*: *Conference Series*, **1684**, Article ID: 012131. https://doi.org/10.1088/1742-6596/1684/1/012131

[5] Bauer, P. (2014) A Simple Landing Gear Simulation Model for Unmanned Aerial Vehicles. *Periodica Polytechnica Transportation Engineering*, **42**, 11-18. https://doi.org/10.3311/pptr.7062

[6] Das, N., Das, S., Mishra, D.K. and Pandey, K.M. (2020) Analysis of Deformation and Mode Shape in the Landing Gear of Light Unmanned Aerial Vehicle. *Journal of Physics*: *Conference Series*, **1455**, Article ID: 012020. https://doi.org/10.1088/1742-6596/1455/1/012020

[7] Zarchi, M. and Attaran, B. (2018) Improved Design of an Active Landing Gear for a Passenger Aircraft Using Multi-Objective Optimization Technique. *Structural and Multidisciplinary Optimization*, **59**, 1813-1833. https://doi.org/10.1007/s00158-018-2135-8

[8] Ding, Z., Wu, H., Wang, C., *et al.* (2019) Hierarchical Optimization of Landing Performance for Lander with Adaptive Landing Gear. *Chinese Journal of Mechanical Engineering* (*English Edition*), **32**, Article No. 20. https://doi.org/10.1186/s10033-019-0331-0
Darmawan, Son, L., Bur, M. and Nurmansyah, (2021) Experimental Studies of Application Passive Momentum Exchange Impact Damper (PMEID) on UAV'S Landing Gear. *IOP Conference Series*: *Materials Science and Engineering*, **1041**, Article ID: 012065. https://doi.org/10.1088/1757-899x/1041/1/012065

[9] Wu, B., Shi, Y. and Yin, Y. (2022) Optimization Design of Landing Gear Structure Based on Fatigue Life Constraint. *Journal of Physics*: *Conference Series*, **2403**, Article ID: 012027. https://doi.org/10.1088/1742-6596/2403/1/012027

[10] Peng, F., Lv, L., Chen, W. and Wang, J. (2023) A Projection-Based Evolutionary Algorithm for Multi-Objective and Many-Objective Optimization. *Processes*, **11**, Article 1564. https://doi.org/10.3390/pr11051564

[11] Harada, T. (2024) Parallel Cooperative Multiobjective Coevolutionary Algorithm for Constrained Multiobjective Optimization Problems. *Applied Soft Computing*, **153**, Article ID: 111290. https://doi.org/10.1016/j.asoc.2024.111290

[12] Tanabe, R. and Ishibuchi, H. (2020) A Review of Evolutionary Multimodal Multiobjective Optimization. *IEEE Transactions on Evolutionary Computation*, **24**, 193-200. https://doi.org/10.1109/tevc.2019.2909744

[13] Borrotti, M., Sambo, F. and Mylona, K. (2023) Multi-Objective Optimisation of Split-Plot Designs. *Econometrics and Statistics*, **28**, 163-172. https://doi.org/10.1016/j.ecosta.2022.04.001

[14] Suo, X., Yu, X. and Li, H. (2017) Subset Simulation for Multi-Objective Optimization. *Applied Mathematical Modelling*, **44**, 425-445. https://doi.org/10.1016/j.apm.2017.02.005

[15] Manson, J.A., Chamberlain, T.W. and Bourne, R.A. (2021) MVMOO: Mixed Variable Multi-Objective Optimisation. *Journal of Global Optimization*, **80**, 865-886. https://doi.org/10.1007/s10898-021-01052-9